Journal Name

ARTICLE TYPE

Cite this: DOI: 00.0000/xxxxxxxxxx

Imaging Defects in Vanadium (III) Oxide Nanocrystals using Bragg Coherent Diffractive imaging

Zachary Barringer,[a] Jie Jiang,[a], Xiaowen Shi[a,b], Elijah Schold[a], Anastasios Pateras[c], S. Cipiccia[d], C. Rau[d], Jian Shi[a], and Edwin Fohtung,*[a]

Received Date
Accepted Date

DOI: 00.0000/xxxxxxxxxx

Defects in strongly correlated materials such as V_2O_3 play influential roles on their electrical properties. Understanding the defects' structure is of paramount importance. In this project, we investigate defect structures in V_2O_3 grown via a flux method. We use AFM to see surface features in several large flake-like particles that exhibit characteristics of spiral growth. We also use Bragg Coherent Diffractive Imaging (BCDI) to probe in 3 dimensions a smaller particle without flake-like morphology and note an absence of the pure screw dislocation characteristic of spiral growth. We identified and measured several defects by comparing the observed local displacement of the crystal, measured via BCDI to well-known models of the displacement around defects in the crystal. We identified two $\vec{b} = \frac{a}{6}[\bar{2}11]$ partial dislocations in the crystal. We discuss how defects of different types influence the morphology of V_2O_3 crystals grown via a flux method.

Transition metal oxides such as vanadium oxides are interesting for a variety of technical applications, from electrochemical anodes[1,2] to unique optical applications[3,4] and supercapacitors.[5] Vanadium (III) oxide (V_2O_3) particularly has been of interest due to its temperature driven first-order metal-insulator phase transition that changes a variety of electronic and optical properties.[6] The properties of vanaduium oxide systems has also been shown to strongly depend on morphology and growth conditions, making it a versatile material for many applications.[7,8]

Defects have been shown to heavily influence a variety of both mechanical and electronic properties of nanoscale materials, which in turn influences their performance in devices.[9–13] In particular, dislocations - while uncommon in nanoparticles - have been shown to affect: lithiation in nanoparticle anodes in Li-ion batteries,[14], optical performance of light emitting diodes,[9] and mechanical deformation of nanostructures.[11,15] The combination of potential nanoscale device application and the dependence of device performance on the type and density of defects results in a need to further understand the formation and control of defects in vanadium oxides, and how defects can influence particle characteristic such as morphology or physical properties.

In this paper we demonstrate a flux method for growing V_2O_3 crystallites. We use transmission electron microscopy (TEM) to analyze the crystal orientation of the crystallites. We use Bragg Coherent Diffractive Imaging (BCDI) to retrieve high-resolution volumetric information about a crystallite showing a significantly different shape than the flake-like particles observed in TEM and optical microscopy. With the BCDI measurements we identified a few partial dislocations with mixed screw and edge character.

BCDI is a technique that circumvents the phase problem of x-ray analytics by over-sampling the diffraction pattern to reconstruct the phase of the diffracted x-rays.[14,16,17] It is used to get high-resolution volumetric information about strain and lattice distortion. In BCDI one reconstructs the phase of the light scattered by a set of crystallographic planes satisfying the Bragg condition. This recovered phase contains information about distortions to the crystal lattice in the direction normal to the diffracting planes. BCDI has been used extensively to map Bragg electronic density, displacement, ferroelectric domains and strain within the volume of crystals with nanoscale resolution;[18–25] the best reported resolution to date is 4-9nm.[26] It has been shown that BCDI can detect signatures of defects by measuring the disruptions to the long-range order of the crystal.[27–30] By examining these long-range effects it is possible to identify defects below the resolution limit of the technique, such as dislocation cores.

We use BCDI in conjunction with AFM, TEM, and optical microscopy to analyze defects in V_2O_3 crystallites grown via flux method. We report on the nature of defects in two different crystallites with different shapes: a flake-like crystallite with features typical of crystals grown via a screw dislocation driven growth mechanism,[31,32] and a smaller particle showing a more complex defect structure, featuring several mixed dislocations. We argue

[a] Department of Materials Science and Engineering, Rensselaer Polytechnic Institute-Troy, New York 12180-3590, USA; E-mail: fohtue@rpi.edu
[b] Department of Physics, New Mexico State University, 1255 N Horseshoe, Las Cruces, NM 88003, USA
[c] Department of Materials Science and Engineering, Carnegie Mellon University, 5000 Forbes Ave, Pittsburgh, PA 15213, USA
[d] Diamond Light Source, Harwell Oxford Campus, Didcot OX11 0DE, United Kingdom

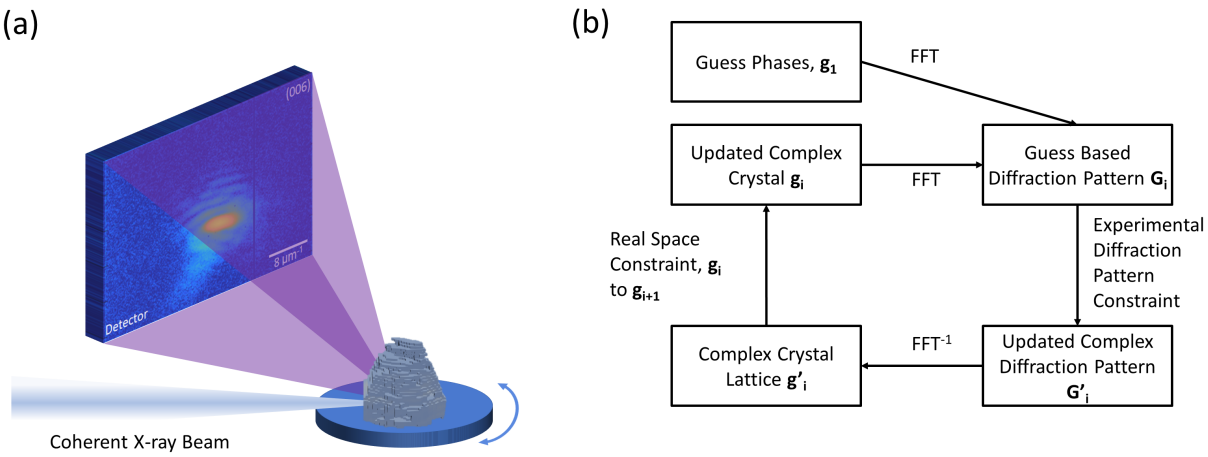

Fig. 1 (a)Diagram of the experimental setup used the BCDI measurements in this work. Coherent x-rays from a synchrotron source are directed to the sample using a Fresnel zone plate (not shown) and is diffracted by a V_2O_3 crystallite. The constructive interference patterns of the diffracted x-rays are recorded while rocking the sample in theta in steps of about 0.001° about the Bragg condition for the (006) peak, effectively measuring the three-dimensional Bragg peak. When the Bragg peak is sufficiently over-sampled, it is possible to apply established phase retrieval algorithms to solve for the complex wave function of the scattered X-rays; a schematic representing the basic form of these phase retrieval algorithm is shown in (b). The retrieved complex scattered wave-function contains information on the Bragg electronic density and lattice displacement of the V_2O_3 crystallite.

that differences in morphology of these particles are potentially a consequence of the different defect structures of the crystals.

1 Methods

V_2O_3 crystals were grown by flux method. A 5 ml graphite crucible containing 0.2 g of V_2O_5 powder and 3.28 g of anhydrous KCl (the mole ratio of V_2O_5:KCl is 1:10) was placed in an alumina tube inside a furnace. The tube was evacuated to 0.1 Torr and then filled with H_2(5%)/Ar gas. A steady flow of 50 sccm H_2(5%)/Ar was maintained throughout the growth at ambient pressure. The crucible was heated at 20°C/min to 900°C and kept for 10 hours and then lowered at 0.5°C/min to ambient. After growth, the contents of the crucible were washed in water (to dissolve the KCl) and black shiny crystals were obtained.

The as-grown crystals were analyzed with optical microscopy, AFM, and BCDI. The optical microscopy was performed using a Nikon Eclipse Ti-S inverted optical microscope to determine the approximate size and shape of the crystals. The AFM measurements were conducted with a MultiModeTM AFM in order to study the topography of the particles. The BCDI was performed at the I13-1 beamline of the Diamond Light Source in order to more closely investigate defects indicated by the AFM measurements.

The diffraction patterns used for BCDI were collected as illustrated in Fig. 1. A monochromatic beam of energy 11.0keV and bandwidth $(\Delta E/E) = 1 \times 10^{-4}$ was focused onto our sample with randomly dispersed (00l)-oriented crystallites. A Fresnel zone plate with diameter of 400μm and outer zone width of 150nm was used to focus the beam. The sample was positioned slightly defocused and downstream of the focusing spot of the Fresnel zone plate, and the final spot size was approximately 2μm full-width at half-maximum and carried a divergence of approximately 50 x 25 μrad. The detector was an Excalibur photon counting direct x-ray detector utilizing a Medipix3 chip, with 55μm x 55μm pixels. The detector was placed in the vicinity of the V_2O_3 (006) Bragg diffraction peak at a distance of approximately 3m from the sample. The sample was scanned to reveal Bragg spots emanating from individual V_2O_3 crystallites. Well isolated Bragg peaks with fringe oscillations indicative of coherent illumination were utilized for this study. Once the Bragg condition was optimized and the sample was positioned to the approximate center of rotation for the sample stage, the stage was rocked in increments of about 0.001° while collecting the diffraction patterns. These few hundred individual diffraction patterns elucidate the 3D structure of the Bragg peak, which encodes the Bragg electronic population and lattice displacement for the reflection.

BCDI is a method for solving the phase problem of x-ray diffraction measurements. In the far field, and assuming the kinematical scattering limit, the scattered amplitude can be expressed as the Fourier transform of a strained crystal. The electron density of such strained crystal is represented by a complex-valued Bragg electron density. When diffracted x-rays are measured, the intensity, I, of the measured x-ray is proportional to the square of this amplitude, as shown in Equation 1.

$$I \propto \left| \int \rho(\vec{r}) * e^{-i\vec{G}_0 \cdot \vec{u}(\vec{r})} * e^{-i\vec{q}\cdot\vec{r}} d\vec{r} \right|^2 \quad (1)$$

Where ρ is the real valued electronic density, $\vec{G}_0$ is the reciprocal lattice vector for a given reflection, $\vec{u}(\vec{r})$ is the displacement field, and $\vec{q} = \vec{k_f} - \vec{k_i}$ is the momentum transfer vector. This shape function (the integrand) is an expression for the location of each atom in the crystal. This basis has an imaginary component that reflects the displacement of the atom from the ideal position of a given crystal projected onto the reciprocal lattice vector. However, the phase component is lost in the measured intensity of an actual x-ray experiment. We algorithmically recover this phase by utilizing an oversampled Bragg peak and repeatedly alternat-

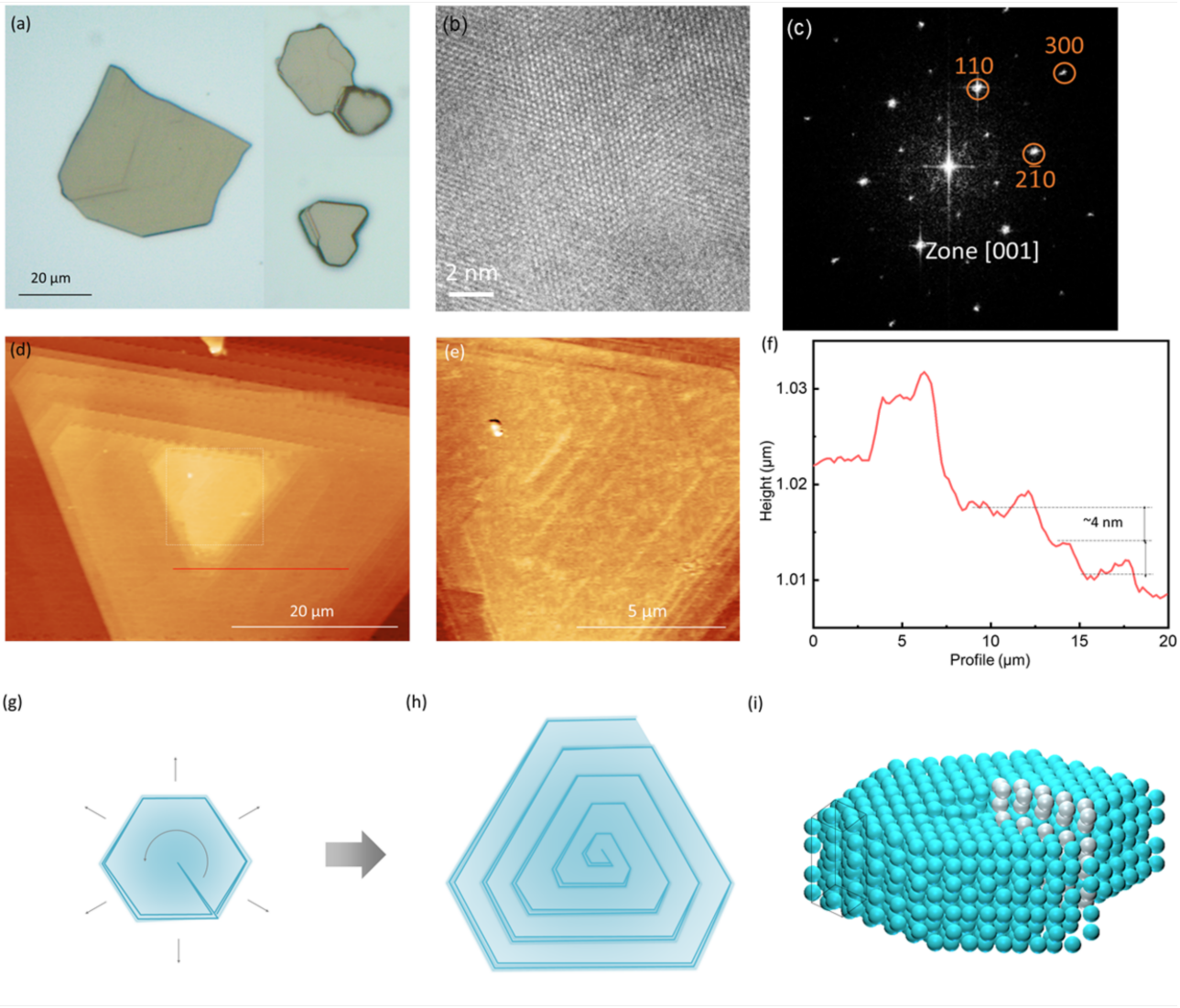

Fig. 2 Morphology, crystal structure and growth mechanism of V_2O_3 microcrystals. (a) Optical image of V_2O_3 flake-like microcrystals. (b) TEM image of a V_2O_3 flake. (c) Electron Fast Fourier Transform (FFT) image with a zone axis [001] of the V_2O_3 flake in (b), conforming the single crystal nature of the flake with the [001] axis normal to its surface. (d),(e) AFM image of a V_2O_3 flake, revealing a screw dislocation driven growth mechanism. (e) is an enlarged view (dashed square) of the screw core in (d). (f) Height profile of the red line in (d), showing an average step height of 4 nm (about three unit cells of V_2O_3). (g),(h) Schematic of the screw dislocation driven growth. The screw dislocation in a nucleus creates a step edge and promotes the growth (curved gray arrow) (g) and eventually a dislocation spiral is formed (h). (i) Schematic of atomic structure of the screw core in V_2O_3 crystal. The initial step edge is indicated as white atoms.

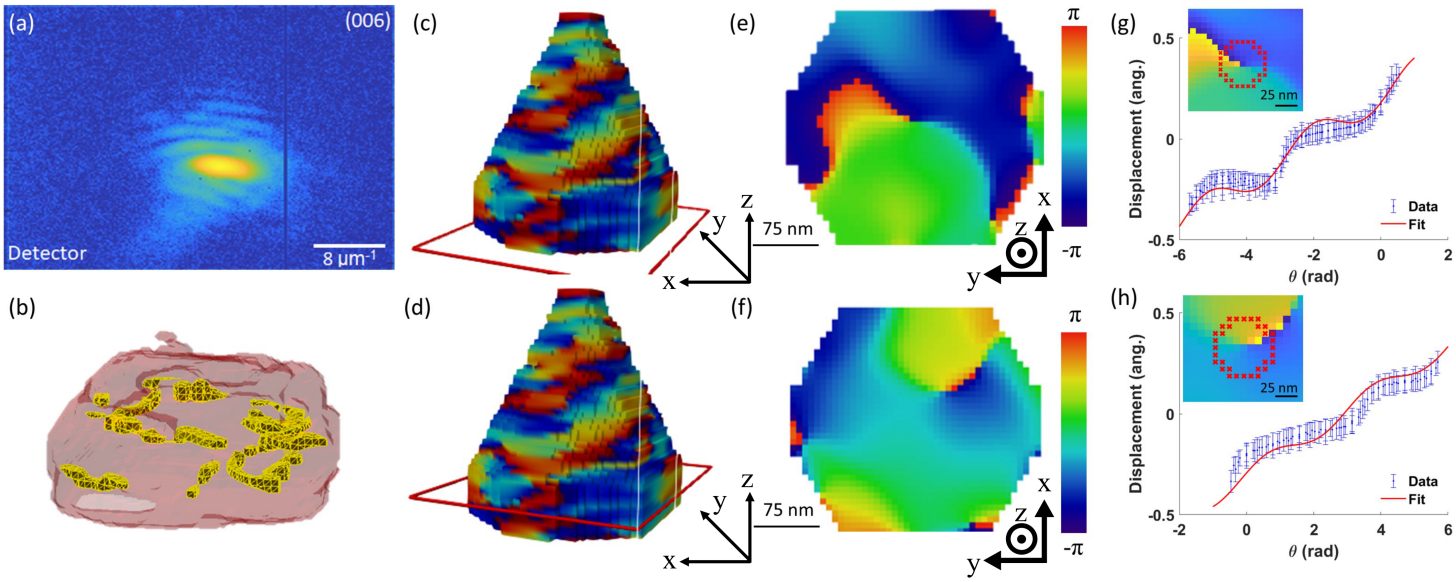

Fig. 3 (a) shows the diffraction peak used for coherent imaging reconstruction. (b) shows the outline of the dislocation cores in the base of the particle, based on the phase of the reconstructed crystal. The displacement is directly proportional to the phase of the reconstructed complex crystal, as shown in Equation 1. The yellow solid lines represent the cores for the mixed and partial dislocations. (c), (d) show the location in the particle of the cross sections shown in (e) and (f) respectively; the color of the images represents the phase of the crystal. The z-coordinate in (c) and (d) points towards [006] direction, and the z-coordinate in (e) and (f) points towards [001] direction. These phase maps show signatures of dislocations, with dislocation lines approximately along [001]. By converting phase to displacement we can determine the Burgers vector of the dislocation. (g), (h) show radial plots of the displacement of the crystal around the dislocation cores, with an inset showing the pixels for one of the radii used for the fitting process.

ing between real and reciprocal space, using inverse and forward Fourier transforms. The algorithm randomly generates a guess of the phase information for the diffraction pattern, and imposes the square-root of the measured intensity values as the amplitude, while the crystal is confined to exist within a finite space (the support). The phase of the diffracted x-ray beam was retrieved using a combination of hybrid input-output and error reduction described by Fienup.[33] Once the phase of the wavefront is retrieved, it is inverse Fourier transformed into a real space complex-valued volume representing the crystallite. The amplitude corresponds to the electronic density population of the Bragg planes, and the phase is the projection of the displacement field onto the momentum transfer vector of the scattering event. The real electronic density reflects the periodicity of the crystallite and the phase is proportional to the displacement of the core electrons from their ideal lattice positions. It is important to note that for highly strained crystals, the kinematic theory cannot always provide adequate results and dynamical approach generalized by Takagi and Taupin[34,35] should be applied. A detailed overview of the dynamical diffraction theory[36,37], and BCDI[16,22,38] is given in a number of works available.

2 Results

The optical microscopy image in Fig. 2a shows three V_2O_3 crystals in different shapes and sizes. The left crystal has a flake-like shape (thin), the right-bottom one has particle-like shape (thick), while the right-up one has a flake and a particle merged together. The angle between the crystal edges are approximately 60 or 120 degree in small crystals (right-up and right-bottom), indicating a hexagonal structure. However, for the large crystal (left), the shape is irregular but there are 120 degree angled step edges on the surface. The lateral size of the crystals are on the order of tens of microns. The TEM image in Fig. 2b shows a thin flake. It is difficult to transfer and locate the same flake from the TEM grid to a substrate for BCDI experiment, however, these samples are likely to have the same crystal structure. Also, they may have different defect (dislocation) densities due to different supersaturation at different regions in the crucible during the growth. The corresponding Fast Fourier Transform (FFT) image in Fig. 2c reveals the α-corundum structure (metal phase) and high crystalline quality of this flake with the [001] axis normal to its surface. Similar geometries have been observed in other materials systems where growth conditions favor spiral crystal growth.[12,31]

The preliminary results showing a suspected dislocation made this material sample an interesting candidate for coherent x-ray imaging. Originally, the sample was selected for Bragg ptychography characterization, another coherent x-ray imaging technique where a sample larger than the beam size is imaged by measuring the diffraction pattern from multiple, overlapping regions of the crystallite. This was due to the size and shape of the particles observed in previous measurements; however, during the experiment we observed a diffraction pattern of a smaller particle - in the size range where BCDI is effective - so we collected data and analyzed this seemingly anomalous particle.

Coherent x-ray imaging is well suited for this application since it creates a map of the atomic displacement with nanoscale resolution. While the resolution is too low to resolve individual atomic positions, it is possible to detect and identify dislocations based on the long-range effect they have on the atomic positions compared to the perfect crystal.

The BCDI reconstruction of the small crystallite showed that the measured crystal was hexagonal, with lateral size around 300 nm, and a height of about 1 micron. The Bragg electron density at the top of the crystal was very low compared to the base of the crystallite. This could potentially be due to the low contribution to the Bragg peak from a very defective portion of the crystal. The phase of this low electron density region has several discontinuities and large gradients, which supports the idea of a very defective crystal. Due to the low Bragg electron density and complicated phase structure, we avoid making claims about the specific crystallographic features present in this portion of the crystal, and it is excluded from the tracing of dislocation cores shown in Fig. 3b.

In the lower region of the crystal, there are several discontinuities in the phase, accompanied by regions of low electronic density. These features are signatures of defects. We used the algorithm published by Ulvestad et al. to estimate the path of dislocations through the crystal.[27] The results of this dislocation tracing are shown in Fig. 3b. This algorithm identifies the path of dislocations by tracing the singularity of the phase around dislocations cores. This technique is unable to identify the path of a dislocation if it lacks this phase signature. Discontinuities in the traced dislocations are likely due to the Burgers vector becoming perpendicular to the momentum transfer of the scattering event used for the reconstruction. This is noteworthy because dislocations must either terminate at the surface of the crystallite or form closed loops,[39] so this is necessarily an incomplete picture of the dislocations in the crystallite.

The results of this algorithm suggest that the defect structure of this small nanoparticle is much more complex than was suspected for the flake-like particle. We attempted to characterize some of the dislocations by fitting the phase to standard models for displacement around an edge dislocation, as previously demonstrated.[14]

The displacement around a dislocation depends on the type of dislocations. Assuming the elastic limit, the displacement around screw dislocations far from the dislocation core can be described as:[39]

$$u_s = \frac{\vec{b}\theta}{2\pi}. \tag{2}$$

All of the displacement is in a single direction, along the direction of the Burgers vector and dislocation line.

Similarly, the displacement around an edge dislocation can be analytically expressed with two components. One component that is perpendicular to the plane of extra atoms and parallel to the Burgers vector:[14]

$$u_\perp = \frac{\vec{b}}{2\pi}\left(\theta + \frac{sin(2\theta)}{4(1-\nu)}\right), \tag{3}$$

and a component parallel to the extra plane of atoms and perpendicular to the Burgers vector:[14]

$$u_{\parallel} = \frac{|\vec{b}|}{2\pi}\left(\frac{1-2\nu}{4(1-\nu)}log(r^2)+\frac{cos(2\theta)}{4(1-\nu)}\right). \quad (4)$$

A displacement field indicative of a dislocation can be seen in Fig. 3e. This feature is not well fit by the equations for edge or screw dislocations; rather its angular dependence is like that of a mixed dislocation, which can be modelled with a combination of edge and screw components:[39]

$$\vec{b} = \vec{b}_e + \vec{b}_s. \quad (5)$$

The displacement was fit at several radii to ensure that the dislocation had been rigorously identified, as previously demonstrated by Ulvestad et al.[14] One angular plot for this mixed dislocations demonstrating the fit of the model is shown in Fig. 3g. The dislocation was well fit by a Burgers vector of $\vec{b} = \frac{a}{6}[\bar{2}11]$, where a is the lattice parameter, with a dislocation line along [001]. The data was well fit by this dislocation, with a root-mean-square-error (RMSE) of 0.035. It is noteworthy that there is a reported partial dislocation in the R$\bar{3}$c crystal structure with a Burgers vector of $\vec{b} = \frac{a}{3}[\bar{2}11]$.[40,41] This mixed dislocation appears to occur where we would expect a screw dislocation to occur in spiral assisted growth. The lack of a pure, perfect screw dislocation here may help explain the discrepancy in particle shape between the large flakes observed in AFM and optical microscopy measurements and the smaller particle measured with BCDI.

The displacement in another portion of the crystal, shown in 3f, was fit using the same technique. One of the circular profiles plotted is shown in Fig. 3h. Using several radii to rigorously identify the dislocation, the Burgers vector was again identified as $\vec{b} = \frac{a}{6}[\bar{2}11]$. The quality of fit for this dislocation is marginally lower than the previous dislocation, with an RMSE of 0.055. This is possibly due to the neighboring dislocations influencing the displacement in the region. In a similar analysis performed by Ulvestad et al. they introduced a correction for neighboring systems of edge dislocations;[14] this correction was not replicated due to the asymmetrical nature of the dislocation system indicating that the neighboring dislocations my not be equal and opposite, and the proximity of the dislocation to the edge of the crystallite making identification using concentric radial plots.

The nature of the dislocations identified in BCDI may provide some insight into the stark contrast between the particle identified in the BCDI measurement and the particles observed with optical and AFM measurements. The presence of a partial dislocation implies the existence of a stacking fault near the base of the crystal; stacking faults have been shown to reduce the energy in thin films,[42] but were only seen in films up to 8-10 nm - much thinner than the particle observed here. The nature of these dislocations could lend insight into the varied morphology of the grown crystallites. Further investigation with BCDI or other techniques could help fully elucidate the role mixed dislocations play in the stunted growth we observed in this system.

3 Conclusions

In summary, we used BCDI to probe the 3D defect structure of a particle, and found a complex defect structure that may have influenced crystal morphology. Our results hint at the role of mixed, partial dislocations in crystal growth. BCDI is a promising tool for investigating the complex role defects have on crystallite morphology. The impact of defect density and type on particle morphology remains a topic of further investigation. Also of potential further interest is what impact these defects or corresponding geometry have on the key properties of V_2O_3, such as the metal-insulator transition.

Conflicts of interest

There are no conflicts to declare.

Acknowledgements

This work was supported by the US Department of Defense, Air Force Office of Scientific Research under Award No. FA9550-14-1-0363 (Program Manager: Dr. Ali Sayir) and funds from Rensselaer Polytechic Institute. The authors would like to acknowledge Diamond Light Source for time on beamline I13-1 under proposal number MT20381-1. J.J and J.S. acknowledge the Air Force Office of Scientific Research under award number FA9550-18-1-0116. E.F. and J.S. acknowledge the National Science Foundation under award no. 2024972.

Notes and references

1 H. Jiang, G. Jia, Y. Hu, Q. Cheng, Y. Fu and C. Li, *Industrial & Engineering Chemistry Research*, 2015, **54**, 2960–2965.

2 L. Jiang, Y. Qu, Z. Ren, P. Yu, D. Zhao, W. Zhou, L. Wang and H. Fu, *ACS Applied Materials & Interfaces*, 2015, **7**, 1595–1601.

3 R. Balu and P. V. Ashrit, *Applied Physics Letters*, 2008, **92**, 021904.

4 M. E. A. Warwick and R. Binions, *J. Mater. Chem. A*, 2014, **2**, 3275–3292.

5 J. Zheng, Y. Zhang, C. Meng, X. Wang, C. Liu, M. Bo, X. Pei, Y. Wei, T. Lv and G. Cao, *Electrochimica Acta*, 2019, **318**, 635–643.

6 G. Andersson, *ACTA Chemica Scandinavia*, 1954, **8**, 1599–1606.

7 Y. Zhang, M. Fan, X. Liu, C. Huang and H. Li, *European Journal of Inorganic Chemistry*, 2012, **2012**, 1650–1659.

8 C. Zheng, X. Zhang, S. He, Q. Fu and D. Lei, *Journal of Solid State Chemistry*, 2003, **170**, 221–226.

9 S. Nakamura, *Science*, 1998, **281**, 956–961.

10 R. Colby, Z. Liang, I. H. Wildeson, D. A. Ewoldt, T. D. Sands, R. E. García and E. A. Stach, *Nano Letters*, 2010, **10**, 1568–1573.

11 J. Godet, P. Hirel, S. Brochard and L. Pizzagalli, *Journal of Applied Physics*, 2009, **105**, 026104.

12 F. Meng, S. A. Morin, A. Forticaux and S. Jin, *Accounts of Chemical Research*, 2013, **46**, 1616–1626.

13 J. Shin, L. Y. Chen, U. T. Sanli, G. Richter, S. Labat, M.-I. Richard, T. Cornelius, O. Thomas and D. S. Gianola, *Acta Materialia*, 2019, **166**, 572–586.

14 A. Ulvestad, A. Singer, J. N. Clark, H. M. Cho, J. W. Kim,

R. Harder, J. Maser, Y. S. Meng and O. G. Shpyrko, *Science*, 2015, **348**, 1344–1347.
15 C. E. Carlton and P. J. Ferreira, *Micron*, 2012, **43**, 1134–1139.
16 D. Karpov and E. Fohtung, *Journal of Applied Physics*, 2019, **125**, 121101.
17 M. C. Newton, S. J. Leake, R. Harder and I. K. Robinson, *Nature Materials*, 2010, **9**, 120–124.
18 F. Hofmann, E. Tarleton, R. J. Harder, N. W. Phillips, P.-W. Ma, J. N. Clark, I. K. Robinson, B. Abbey, W. Liu and C. E. Beck, *Scientific Reports*, 2017, **7**, 1–10.
19 D. Karpov, Z. Liu, T. d. S. Rolo, R. Harder, P. V. Balachandran, D. Xue, T. Lookman and E. Fohtung, *Nature Communications*, 2017, **8**, 280.
20 S. Labat, M.-I. Richard, M. Dupraz, M. Gailhanou, G. Beutier, M. Verdier, F. Mastropietro, T. W. Cornelius, T. U. Schülli, J. Eymery and O. Thomas, *ACS Nano*, 2015, **9**, 9210–9216.
21 X. Shi, R. Harder, Z. Liu, O. Shpyrko, E. Fullerton, B. Kiefer and E. Fohtung, *Crystals*, 2020, **10**, 658.
22 R. Harder and I. K. Robinson, *Jom*, 2013, **65**, 1202–1207.
23 A. Minkevich, E. Fohtung, T. Slobodskyy, M. Riotte, D. Grigoriev, M. Schmidbauer, A. Irvine, V. Novák, V. Holỳ and T. Baumbach, *Physical Review B*, 2011, **84**, 054113.
24 A. Pateras, R. Harder, S. Manna, B. Kiefer, R. L. Sandberg, S. Trugman, J. W. Kim, J. de la Venta, E. E. Fullerton, O. G. Shpyrko and E. Fohtung, *NPG Asia Materials*, 2019, **11**, 1–7.
25 Z. Liu, E. Schold, D. Karpov, R. Harder, T. Lookman and E. Fohtung, *Advanced Electronic Materials*, **n/a**, 1901300.
26 M. J. Cherukara, W. Cha and R. J. Harder, *Applied Physics Letters*, 2018, **113**, 203101.
27 A. Ulvestad, M. Menickelly and S. M. Wild, *AIP Advances*, 2018, **8**, 015114.
28 J. N. Clark, J. Ihli, A. S. Schenk, Y.-Y. Kim, A. N. Kulak, J. M. Campbell, G. Nisbet, F. C. Meldrum and I. K. Robinson, *Nature Materials*, 2015, **14**, 780–784.
29 M. Dupraz, G. Beutier, T. W. Cornelius, G. Parry, Z. Ren, S. Labat, M.-I. Richard, G. A. Chahine, O. Kovalenko, M. De Boissieu, E. Rabkin, M. Verdier and O. Thomas, *Nano Letters*, 2017, **17**, 6696–6701.
30 A. Yau, W. Cha, M. W. Kanan, G. B. Stephenson and A. Ulvestad, *Science*, 2017, **356**, 739–742.
31 A. G. Shtukenberg, Z. Zhu, Z. An, M. Bhandari, P. Song, B. Kahr and M. D. Ward, *Proceedings of the National Academy of Sciences*, 2013, **110**, 17195–17198.
32 W. K. Burton, N. Cabrera, F. C. Frank and N. F. Mott, *Philosophical Transactions of the Royal Society of London. Series A, Mathematical and Physical Sciences*, 1951, **243**, 299–358.
33 J. R. Fienup, *Applied Optics*, 1982, **21**, 2758–2769.
34 S. Takagi, *Acta Crystallographica*, 1962, **15**, 1311–1312.
35 S. Takagi, *Journal of the Physical Society of Japan*, 1969, **26**, 1239–1253.
36 A. Authier, *International Tables for Crystallography*, 2006, 626–646.
37 Z. G. Pinsker, 1978.
38 H. Quiney, G. Williams and E. Fohtung, *Journal of Optics*, 2017, **20**, 010201.
39 D. Hull and D. Bacon, *Introduction to Dislocations*, Elsevier, 2011.
40 N. Shibata, M. F. Chisholm, A. Nakamura, S. J. Pennycook, T. Yamamoto and Y. Ikuhara, *Science*, 2007, **316**, 82–85.
41 B. Miao, S. Kondo, E. Tochigi, J. Wei, B. Feng, N. Shibata and Y. Ikuhara, *Scripta Materialia*, 2019, **163**, 157–162.
42 Y. Liu and L. Li, *Nanotechnology*, 2011, **22**, 425707.